Accurate computation of chemical contrast in field ion microscopy

Shalini Bhatt, Shyam Katnagallu, Jörg Neugebauer, and Christoph Freysoldt
Max-Planck-Institut für Eisenforschung GmbH, Düsseldorf, Germany

We present a computational approach to simulate local contrast observed in Field Ion Microscopy (FIM). It is based on density-functional theory utilizing the Tersoff-Hamann approach as done in Scanning Tunneling Microscopy (STM). A key requirement is the highly accurate computation of the surface states' wave-function tails. To refine the Kohn-Sham states from standard iterative global solvers we introduce and discuss the **EX**trapolation of **T**ails via **R**everse integration **A**lgorithm (EXTRA). The decaying tails are obtained by reverse integration (from outside in) using a Numerov-like algorithm. The starting conditions are then iteratively adapted to match the values of plane-wave Kohn-Sham wave functions close to the surface. We demonstrate the performance of the proposed algorithm by analysing and showing the chemical contrast for Ta at Ni surface.

I. INTRODUCTION

Field ion microscopy (FIM) was the first microscopy technique that was able to image individual atoms on a metal surface with atomic spatial resolution[1, 2]. The imaging gas (e.g. He, Ne) is ionized above a surface of a nano-sharp needle-shaped specimen (end diameter $< 100\,\mathrm{nm}$) subject to a high electric field of 10^{10} V/m. The ions are then accelerated along the field lines and hit a two-dimensional detector to produce an image magnified by a factor of 10^7 [3]. Even though field ion microscopy as a surface characterization method has largely been superseded by scanning tunneling microscopy [4], atomic force microscopy and similar scanning probe techniques[5], there has been a recent revival when combined with field evaporation (3D-FIM) [6–8] as one of the few techniques that can image crystallographic features with atomic resolution in three dimensions. FIM was used to provide insights into crystallographic defects such as vacancies[8–10], dislocations, or voids [11, 12]. However, the quantitative interpretations of imaging contrast enabled by theory have been sparse [13]. Numerous studies have focused on understanding the image contrast in field ion image [14–16].

Under best imaging field conditions, the local imaging contrast is dominated by the ionization probability at 5-10 Å above the surface [17]. Ionization near the surface requires an electron transfer from the gas atom into an empty surface state. Without an electrostatic field, this would be energetically impossible since the ionization level of the imaging gas (≈15-25 eV) exceeds the work function (≈3-6 eV for most metals). The electric field provides the required voltage drop to overcome this difference and to enable electron tunneling when the gas atom is beyond a critical distance away from the surface. To simulate this within density-functional theory (DFT), we adopt Tersoff-Hamann theory known from scanning tunneling microscopy (STM)[18] for tunneling between a real surface and probe tip. In their ground-breaking work, Tersoff and Hamann found the tunneling current to be proportional to the surface local density of states (LDOS) near the Fermi level at the position of the tip in STM. Their derivation equally applies when the spherical tip is replaced by a single atom.

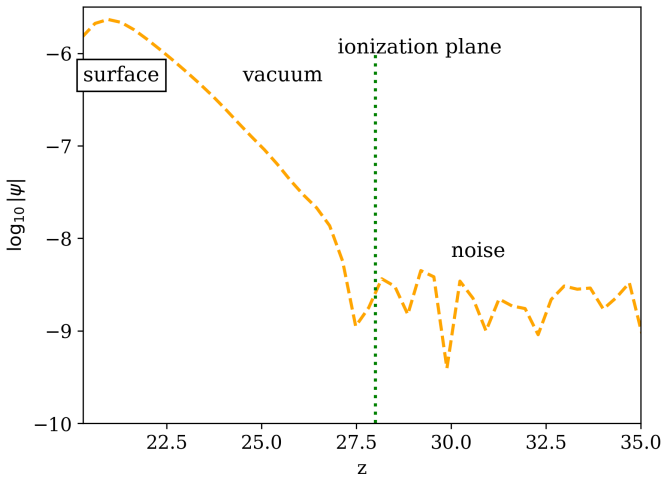

FIG. 1: Typical evolution of numerical wave functions on top of Ta in a Ni(012) surface in the presence of an electric field as obtained from a standard DFT code. The decay behavior of the wave function (orange curve) is shown for an eigenvalue at the Fermi level. For FIM image contrast, ψ is needed at the ionization plane.

Both STM and FIM use electron tunneling for forming an image of a solid surface. However, the field strength in FIM is higher than in STM, so explicit fields must be considered in simulations [11, 19]. Our previous work [11] has applied the Tersoff-Hamann (TH) approximation in DFT simulations to explain the brighter appearance of Re atoms during FIM imaging of a Ni-Re alloy, focusing on states right above the Fermi level. While such a selective approach explained the chemical contrast in this case, the numerical accuracy in other cases emerged as a critical issue as discussed below, which limits its application.

The computational challenge in these calculations is that the high electric field leads to a very fast decay of wave functions into the vacuum. When we employed the Tersoff-Hamann approach for a wider range of cases, we found that the accuracy of wave functions from standard DFT is often insufficient to make quantitative predic-

tions for FIM, as sketched in Fig. 1. The standard wave-function optimization algorithms implemented in plane-wave DFT codes are based on the Rayleigh-Ritz method of minimizing the (global) norm of the residue[20]. This implies that the highest magnitude in the wave function determines the global algorithm's notion of 'large' and 'small'. Hence, they give the best relative accuracy where the wave function amplitude is large. On the downside, in areas where the wave function is small in magnitude, the relative error between the approximate solution and the exact solution can become excessively large even if the total residue is at the numerical limit. The electrostatic field present in FIM further leads to a strong, non-exponential decay of wave functions and they run into a regime where noise dominates.

The main idea of the present work is to recompute the tails of the wave functions with an algorithm that works at the local scale. More precisely, we develop an algorithm that is local with respect to the dominant direction for scale (in the following: z), i.e., away from the slab surface. For this, we assume that the eigenvalues ϵ_i and corresponding eigenfunctions $\psi_i(\mathbf{r})$ close to the slab have been reliably computed. Then, the task is to integrate the underlying second-order differential equation i.e the Kohn-Sham equation from this trusted region along the z direction.

The rest of this article is organized as follows. In Sec. II, we will present our tail extrapolation scheme and show that it is robust even if the wave function amplitude varies over 10 or more orders of magnitude along the direction of integration. In Sec. III we apply the new algorithm to a prototype surface the Ni(012) containing substitutional Ta atoms, and show that we can successfully reproduce the enhanced brightness observed in experiment [21].

II. EXTRAPOLATION OF TAIL VIA REVERSE INTEGRATION ALGORITHM (EXTRA)

A. Reverse Integration

In DFT, the Kohn-Sham equation reads[22]

$$\left(-\frac{1}{2}\nabla + V_{\text{eff}}(\mathbf{r})\right)\psi_i(\mathbf{r}) = \epsilon_i\psi_i(\mathbf{r}) \tag{1}$$

using Hartree atomic units ($\hbar$=1, m_e=1, $4\pi\epsilon_0$=1). The effective potential is obtained as

$$V_{\text{eff}} = V_{\text{ext}} + V_{\text{H}} + V_{\text{xc}} \ . \tag{2}$$

The external potential V_{ext} defines the Coulomb interaction between an electron and the collection of atomic nuclei. The Hartree potential V_{H} describes the classical Coulomb repulsion between the electrons, and the exchange-correlation potential V_{xc} encompasses quantum mechanical corrections. In common density-based approximations (e.g. LDA, GGA, meta-GGA), V_{xc} depends on the local density and vanishes as the density becomes zero. The vacuum potential is therefore dominated by the electrostatic potential $V_{\text{ext}} + V_{\text{H}}$.

Rewriting Eq. (1) as

$$\frac{1}{2}\frac{\partial^2}{\partial z^2}\psi_i(\mathbf{r}) = \left\{-\frac{1}{2}\left(\frac{\partial^2}{\partial x^2} + \frac{\partial^2}{\partial y^2}\right) + V_{\text{eff}}(\mathbf{r}) - \epsilon_i\right\}\psi_i(\mathbf{r}) \tag{3}$$

provides the basis to numerically integrate the wave function ψ_i along the z-direction. For the sake of readability, we will omit the state index i from the equations in the following.

It is well known from the theory of second-order differential equations in one dimension (1D) that there are two linearly independent solutions. In our case, a decaying and a rising solution are possible. In forward integration the decaying solution is always challenging to compute because numerical noise (e.g. rounding errors due to the finite precision) can produce a small contribution of the rising solution, which then grows as the algorithm proceeds and ultimately dominates.

To circumvent this problem, one can reverse the direction of integration: by starting deep in the vacuum and integrating towards the surface, the desired solution is growing in magnitude and thus can be easily computed. In consequence, the extrapolation problem is turned into a problem of choosing starting conditions such that the integrated tail solution matches the values of the global optimization near the surface, in our case at the matching plane $z = z_{\text{match}}$.

Before we come to the integration algorithm, let us briefly review the key properties of the effective potential. In a vacuum, where the density becomes negligibly small, the electrostatic part becomes dominant and V_{xc} vanishes. Hence, it is interesting to understand how the electrostatic potential develops far away from the surface. For this, one can apply a Fourier transform in the xy plane [with wave vector $\mathbf{k} = (k_x, k_y)$] to a 'mixed-space' representation $V(\mathbf{k}, z)$. As shown in Appendix A, the xy-averaged electrostatic potential is constant or diverges linearly along z, while the lateral potential variations decay exponentially. Hence, beyond a certain point, the xy-averaged potential will strongly dominate the evolution of the wave functions along z. We, therefore, de-

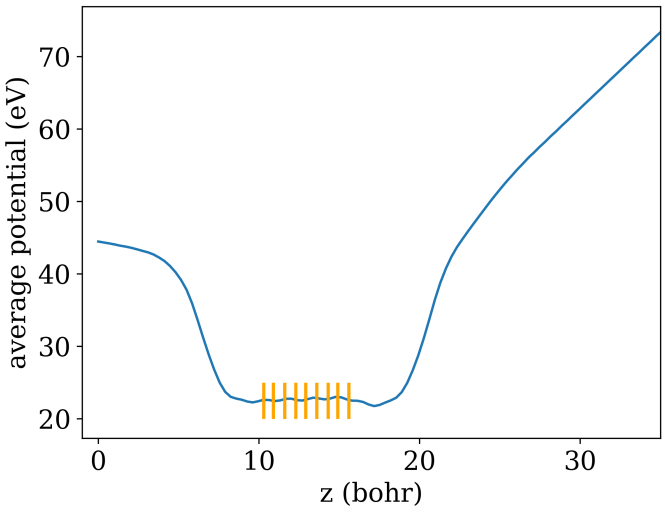

FIG. 2: The effective potential along z averaged over xy plane of a charged Ta-Ni(012) slab with 9 atomic layers (as shown in orange vertical lines). An electric field of 40 V/nm is applied at the top side.

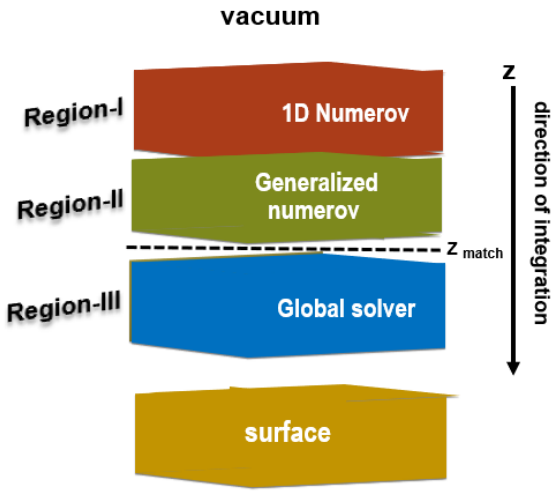

FIG. 3: Algorithm applied to the various regions above the surface. The reverse integration in z starts from the top to the bottom (z_{match}). In region I the 1D Numerov solution is computed. In region II the novel EXTRA algorithm is applied. Region III contains the unmodified plane-wave wave functions obtained from the global solver (plane-wave DFT code).

compose the potential

$$V(x,y,z) = \overline{V}(z) + \delta V(x,y,z) \tag{4}$$

into the average potential $\overline{V}$ for $k_x = k_y = 0$ component and the lateral variation δV for $|\mathbf{k}| > 0$. Fig. 2 shows the average potential obtained from DFT calculations discussed in Sec. III.

B. Overview of tail extrapolation

In our algorithm, we split the space above the surface into three regions, named regions I, II, and III from outside in, as shown schematically in Fig. 3. Region III, closest to the surface, is where the DFT program's global solver provides sufficiently accurate numerical wave functions and hence does not require additional optimization. For simplicity, we define region III below a plane parallel to the surface, at height z_{match}. Region I is far away from the slab, where the lateral variations of the potential are negligible. As shown in Sec. II C, this simplification renders the Kohn-Sham equation separable in the mixed space within region I, and allows us to use 1D Numerov integration along z as an efficient and accurate algorithm to compute wave-function tails. Closer to the slab, in region II, lateral variations in the potential become important and the 1D Numerov would be inaccurate. We therefore generalized the Numerov algorithm to three dimensions (see Appendix B) to perform integrations in region II. In Sec. II D we show that this must be combined with Fourier-filtering in mixed space to ensure robustness over many orders of magnitude for the wave-function amplitude. In practice, our Fourier filtering can be seen as introducing a curved boundary in mixed $(\mathbf{k}, z)$ space between region I and region II.

The key task to ensure a coherent wave function across all three regions is to make the separately computed wave functions match at the region I/region II and the region II/region III boundaries, respectively. For the former, this is readily achieved by rescaling, see Sec. II C below. For the latter, where the region III wave functions are authorative, we employ an iterative procedure summarized in Sec. II E. As the I/II boundary values serve as starting values for region II reverse integration towards region III, we vary these boundary values to minimize mismatch at the II/III boundary. The combined approach, i.e., 1D integration in region I (Sec. II C), Fourier-filtered generalized Numerov integration in region II (Sec. II D), and the iterative procedure for determining the I/II boundary values as the key unknowns in wave-function matching (Sec. II E), is termed EXTRA (**EX**trapolation of **T**ails via **R**everse integration **A**lgorithm).

C. Region I: 1D Numerov integration in mixed space

Deep in vacuum, δV becomes negligible, and Eq. (4) reduces to

$$V(x,y,z) \approx \overline{V}(z)\ . \tag{5}$$

Within this approximation, an in-plane Fourier transform makes the Kohn-Sham equation, Eq. (3), separable

in **k** and z, i.e., in mixed space

$$\frac{1}{2}\frac{\partial^2\psi(\mathbf{k},z)}{\partial z^2} = \left\{\frac{1}{2}|\mathbf{k}|^2 + \overline{V}(z) - \epsilon\right\}\psi(\mathbf{k},z) \qquad (6)$$

with both growing and decaying solutions if $\epsilon < \overline{V}(z)$ for all z. For recomputing the decaying tails, 1D Numerov is a feasible algorithm [23, 24]. For this, one performs reverse Numerov integration, starting deep in the vacuum with arbitrary non-vanishing initial values, and rescales the intermediate solution such that it matches a given value $\psi(\mathbf{k}, z_{\text{start}})$ at the boundary z_{start} between regions I and II.

The Numerov method is a finite difference method that calculates the shape of the wave function by integrating step-by-step along a grid. The one dimensional Schrödinger equation is solved using Numerov algorithm[25] in form of

$$\psi_{n+1} = \frac{2(1-\frac{5}{12}h^2k_n^2)\psi_n - (1+\frac{1}{12}h^2k_{n-1}^2)\psi_{n-1}}{1+\frac{1}{12}h^2k_{n+1}^2} \qquad (7)$$

where

$$k_n^2 = 2\epsilon - 2\overline{V}(z_n) - |\mathbf{k}|^2 \ . \qquad (8)$$

There are different variants of Numerov [26, 27] developed in the past for the approximate solution of Schrödinger equation. The discretization error of the Numerov algorithm is $\mathcal{O}(h^6)$.

The numerical accuracy of the Numerov algorithm for rising solutions over many orders of magnitude arises from the locality: only the previous two values are needed, and these lie at a very similar magnitude. Uncorrelated numerical round-off errors cannot grow faster than the exact solution, because they either are proportional to the desired solution or belong to the linearly independent, decaying solution. This also ensures that starting from arbitrary values will always converge towards the rising solution after a warmup phase.

D. Region II: Fourier-filtered generalized Numerov integration

1. *Generalized Numerov algorithm*

In order to numerically integrate the 3D Schrödinger equation along the z direction, we propose a generalized Numerov algorithm given in Appendix B. The working equation is [cf. Eq. (B6)]

$$\begin{aligned}\left[1+\frac{1}{6}h^2\left\{\epsilon-\hat{V}(z_{n+1})\right\}\right]\psi_{n+1} \\ = 2\left[1-\frac{5}{6}h^2\left\{\epsilon-\hat{V}(z_n)\right\}\right]\psi_n \\ -\left[1+\frac{1}{6}h^2\left\{\epsilon-\hat{V}(z_{n-1})\right\}\right]\psi_{n-1}\end{aligned} \qquad (9)$$

Eq. (9) represents an in-plane partial differential equation [with linear operator $\hat{V}(z)$] for ψ_{n+1} with a known right-hand side that depends on the values for the two previous steps z_n and z_{n-1}. By solving this differential equation numerically using a standard (plane-global) iterative algorithm, one can step-wise proceed along the z direction. The in-plane kinetic operator is computed in mixed space, while the potential is applied in real space, using fast Fourier transforms to switch between these two spaces. To solve the discretized differential equation, we employ the root finding solver of the Scipy optimization module[28] (scipy.optimize.root) with Krylov subspace iterations [29] and a numerical approximate inverse Jacobian.

The key advantage of this procedure is that the numerical solver of the in-plane equation must only deal with scale variations within the plane, while the huge changes in magnitude along the z direction are taken care of by the explicit iteration $(\psi_{n-1}, \psi_n) \to \psi_{n+1}$.

2. *High-frequency noise issues with unfiltered generalized Numerov*

We have tested the Generalized Numerov numerical integration in the reverse direction in a region near the surface where the global solver provides a nicely decaying reference solution.Generalized Numerov is stable against numerical noise from the unwanted solution (i.e., the exponential rising solution into vacuum). Unfortunately, when integrating towards the surface, it produces a rapid increase of contributions from high-frequency Fourier components in the plane that are absent from the reference solution. This is not a failure in principle, as we can expect from the separable approximation, Eq. (6) that in-plane frequency coefficients for high **k** values have steeper slopes along z compared to the low-frequency ones as shown in Fig. 4. Yet, this makes the Generalized Numerov algorithm of Appendix B sensitive to high-frequency noise.

The reason behind the discrepancy is visualized in Fig. 4 which illustrates how the wave-function magnitude develops for different k values. As shown in Fig. 5, iso-magnitude contours in mixed (k_x, k_y, z) space are not parallel to the (k_x, k_y) plane. In consequence, we find that it is not sufficient to find an algorithm that has a local scale in only z, but actually, one that respects the local scale in (k_x, k_y, z). To circumvent the above issue, we additionally employ a z-dependent Fourier filtering in the xy plane. The challenge is to distinguish between noise and the true signal. Fortunately, for each mixed-space coefficient, we can estimate the expected magnitude relative to the matching plane from the 1D separable equation, Eq. (6). We can use this to make a Fourier-filtering at "equal magnitude".

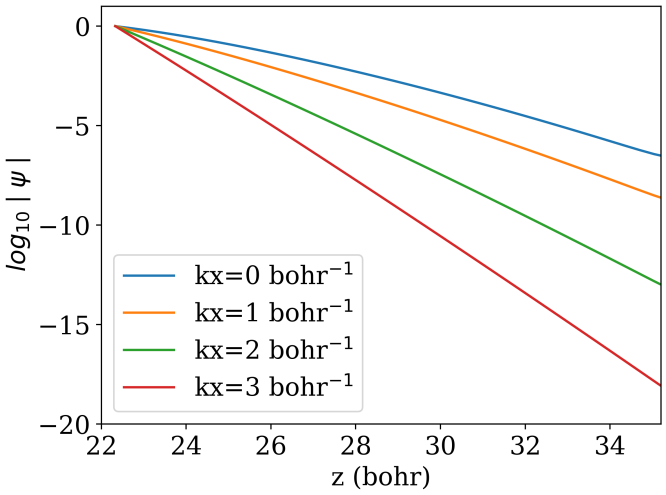

FIG. 4: 1D Numerov wave-function magnitude as a function of z using the potential shown in Fig. 2. The decay rate depends on in-plane Fourier components k_x. The wave functions are calculated for an eigenvalue at the Fermi level and normalized with respect to z_{match}=22 bohr.

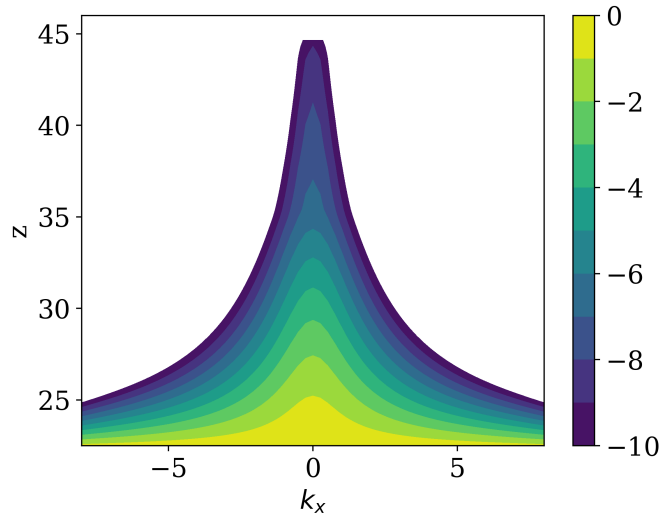

FIG. 5: Iso-magnitude contours of Ta-Ni(012) plotted in mixed space. The wave functions were generated from 1D Numerov using the average potential (see Fig. 2), and were normalized with respect to z_{match}=22 bohr.

3. *The iso-magnitude boundary for regions I/II*

At the boundary between region II/region III high frequency fourier components obtained by the Generalized Numerov algorithm grow rapidly and need to be filtered out. To do this we make the boundary k-dependent using the iso-magnitude condition

$$\psi_{1d}(\mathbf{k}, z_{\text{start}}(\mathbf{k}))/\psi_{1d}(\mathbf{k}, z_{\text{match}}) = \eta \qquad (10)$$

where η defines the magnitude threshold. Eq. (10) defines a finite $z_{\text{start}}(\mathbf{k})$ beyond which the coefficients can be effectively ignored (set to zero) for the generalized Numerov step as shown in Fig. 5. The choice of η is not overly problematic in practice. We have successfully employed values of 10^{-6}, 10^{-8}, and even 10^{-20} and observed negligible differences between the results. If η is chosen too small, high-frequency noise occurs. If chosen too large, the original DFT wave functions are not well reproduced near the matching plane (where the intrinsic noise is small).

The values $\psi(\mathbf{k}, z_{\text{start}}(\mathbf{k})) = \psi_{\text{start}}(\mathbf{k})$ are used as the initial conditions for the generalized Numerov integration. They fully determine the shape of the wave function inside region II. For initializing the previous value we use 1D Numerov to estimate $\psi(\mathbf{k}, z_{\text{start}}(\mathbf{k})-h)$. Similarly, we use 1D Numerov to extend ψ beyond the filtering boundary in an approximate way namely ignoring the effect of in-plane scattering due to the in-plane potential variant ions δV.

In this way, the iso-magnitude contour is effectively treated as our dividing boundary between region I and region II in mixed space. At this boundary, we initialize the Fourier components for the region II integration. In short only coefficients inside the boundary are included in the generalized Numerov for region II. Outside this contour boundary, i.e., in the region I, we rescale the precomputed 1D Numerov solutions to match the boundary value.

We note in passing that we can combine the iso-magnitude boundary condition with a maximum for z_{start} based on the in-plane lateral variations δV. In such a case, we cap the contour when the lateral variations become negligible, and thus the 1D Numerov integration is accurate (and far more efficient).

4. *Fourier filtered generalized Numerov*

To summarize the Fourier-filtered generalized Numerov, the iteration proceeds as follows.

1. Given $\psi(\mathbf{k}, z_{n-1})$ in mixed space and $\psi(x, y, z_n)$ in real space on a regular discretization grid, Fourier transform the latter one to mixed space via Fast Fourier transforms (FFT).

2. Set $\psi(\mathbf{k}, z_n)$ to zero where $z_n > z_{\text{start}}(\mathbf{k})$.

3. For cases at the boundary, where $z_n = z_{\text{start}}$, set

$$\psi(\mathbf{k}, z_n) = \psi_{\text{start}}(\mathbf{k})$$
$$\psi(\mathbf{k}, z_{n-1}) = \psi_{\text{start}}(\mathbf{k}) \cdot \frac{\psi_{1d}(\mathbf{k}, z_{n-1})}{\psi_{1d}(\mathbf{k}, z_n)} .$$

4. Save $\psi(\mathbf{k}, z_n)$ for the next iteration.

5. Fourier transform both $\psi(\mathbf{k}, z_{n-1})$ and $\psi(\mathbf{k}, z_n)$ to real space.

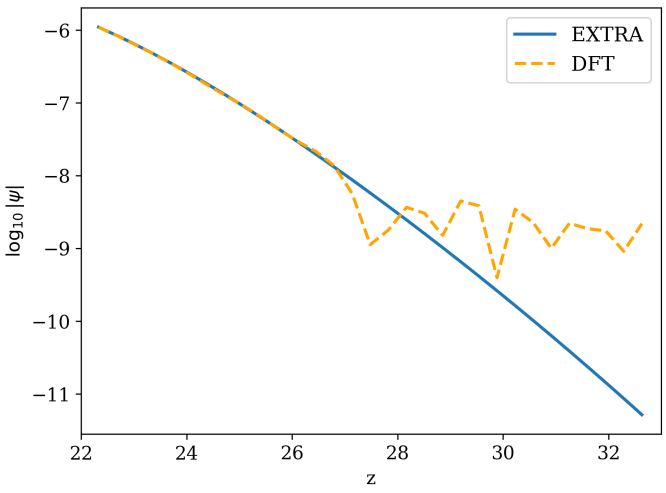

FIG. 6: Comparison of computed wave-functions of Ta-Ni(012) along the direction z. The wave functions are calculated for an eigenvalue at the Fermi level. The position of the matching plane where both curves agree is $z_{\mathrm{match}} = 22\,\mathrm{bohr}$.

6. Perform generalized Numerov propagation by solving Eq. (9), yielding the real-space for the next iteration z_{n+1}.

When z_{match} has been reached, the missing region I tails are added to the mixed-space representation by setting

$$\psi(\mathbf{k}, z_n) = \psi_{\mathrm{start}}(\mathbf{k}) \cdot \frac{\psi_{1d}(\mathbf{k}, z_n)}{\psi_{1d}(\mathbf{k}, z_{\mathrm{start}}(\mathbf{k}))} \tag{11}$$

for all $z_n > z_{\mathrm{start}}(\mathbf{k})$. Afterward, the real-space representation can be recomputed from this via in-plane FFTs.

E. Iterative determination of ψ_{start}

The final step is to determine the starting values $\psi_{\mathrm{start}}(\mathbf{k})$ such that integration across region II according to the algorithm described above yields values $\psi_{II}(x, y, z_{\mathrm{match}})$ at the matching plane that agree with the desired values. These values are given by the original DFT wave function in region III, i.e., by $\psi_{III}(x, y, z_{\mathrm{match}})$.

For this purpose, we define the residue

$$R(\mathbf{k}) = \psi_{III}(\mathbf{k}, z_{\mathrm{match}}) - \psi_{II}(\mathbf{k}, z_{\mathrm{match}}) \tag{12}$$

that implicitly depends on $\psi_{\mathrm{start}}(\mathbf{k})$. We then solve the multidimensional root-finding problem $R = 0$, treating R as a function of ψ_{start}. However, there is a huge difference in magnitude between the residue R (which is similar in scale to the wave function at the matching plane), and the starting values ψ_{start} at the iso-contour boundary. The latter are smaller by a factor η, cf. Eq. (10). To accommodate for the scale, we iterate on

$$\psi_{\mathrm{init}}(\mathbf{k}) = \psi_{\mathrm{start}}(\mathbf{k}) \cdot \frac{\psi_{1d}(\mathbf{k}, z_{\mathrm{match}})}{\psi_{1d}(\mathbf{k}, z_{\mathrm{start}}(\mathbf{k}))}\,. \tag{13}$$

ψ_{init} can be thought of as the boundary values rescaled to the matching plane via the 1D Numerov approximation. We use this flexible definition rather than the constant η to accommodate situations in which we limit $z_{\mathrm{start}}(\mathbf{k})$ to a maximum based on the magnitude of δV, as explained in Sec. II D 3. The root finding algorithm, *scipy.optimize.root* with Krylov iteration and numerical inverse Jacobian estimation [29], is then used to solve for the starting values, completely analogous to our solution of the generalized Numerov propagation, Eq. (9), see Sec. II D 1. Fig. 6 illustrates the comparison of the original, noisy wave function from the global DFT solver with one from EXTRA on the log scale. It demonstrates that EXTRA overcomes the limitations of the global solution.

III. INVESTIGATION OF SUBSTITUTIONAL TA IN NI

In this Section, we will illustrate that the EXTRA algorithm allows us to overcome the accuracy limitations that prevented direct simulations of FIM contrast. For this, we choose the case of substitutional Ta in Ni. In a recent a-FIM study with Ne as an imaging gas, Morgado *et al.* investigated segregation in Ni alloys with 2% Ta [21]. They observed that Ta was imaged in FIM more brightly than Ni. This finding was qualitatively explained by DFT calculations performed by some of the present authors. The DFT calculations showed that Ta-related states appear energetically at 1-3 eV above the Fermi level, while only a few Ni states in the spin minority channel are available for tunneling electrons up to 1 eV above the Fermi level. However, due to the accuracy limitations, it was not possible to actually compute the FIM contrast at relevant ionization energies, nor to verify that Ta-related states at higher energies give at all a brighter signal than the lower-lying Ni states. In the present work, DFT was performed in the plane-wave PAW formalism with the SPHInX code [30] using the Perdew-Burke-Ernzerhof (PBE) exchange-correlation functional [31] with D2 van-der-Waals corrections[32]. The calculation was spin-polarized with colinear spin and produces a ferromagnetic state. The Ni (012) surface was modeled in the repeated slab approach with 9 atomic layers at the theoretical lattice constant (3.465 Å) and a vacuum separation of 17.5 Å. An electric field of 40 V/nm was included via the generalized dipole correction [19]. Tantalum substitution at the surface was modeled in a 3×3 surface unit cell, i.e, with 9 surface atoms as shown in Fig. 7. The 6 topmost layers were relaxed via quasi-Newton optimization with a redundant internal coordinated Hessian fitted on the fly [33] until the forces were below 0.015 eV/Å. For the structure optimization, an offset $2 \times 3 \times 1$ **k**-point sampling was used, equivalent to a

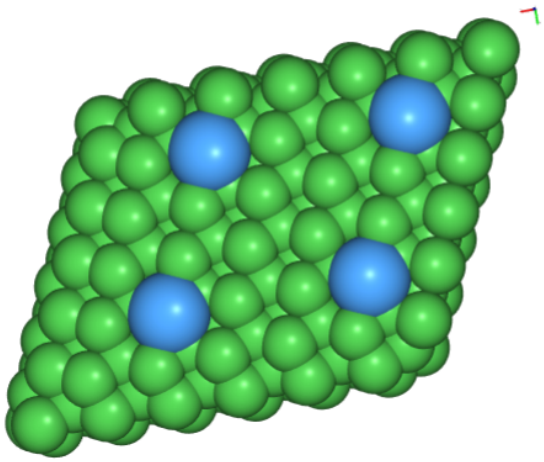

FIG. 7: Top view of Ta-Ni(012) where Tantalum (blue) is surrounded by Nickel (green). The 3×3 surface cell has been duplicated in both directions for clarity.

k-point spacing of $0.13\,\mathrm{bohr}^{-1}$. For the DOS calculation, the **k**-point density in the plane was doubled ($4 \times 6 \times 1$).

The partial DOS at energy E is given by

$$\rho(\mathbf{r}, E) = \sum_{i\sigma\mathbf{k}} w_{\mathbf{k}} |\psi_{i\sigma\mathbf{k}}(\mathbf{r})|^2 \delta(E - \epsilon_{i\sigma\mathbf{k}}) \qquad (14)$$

for state index i and spin index σ. $w_{\mathbf{k}}$ denotes the **k**-point weight. To turn this into a two-dimensional FIM contrast map, we impose energy conservation for the tunneling process, i.e.,

$$E = \epsilon_{i\sigma\mathbf{k}} = V_{\mathrm{avg}}(x, y, z) - I \;, \qquad (15)$$

where I is the (positive) ionization energy of the imaging gas. V_{avg} is the average potential that the imaging gas atom experiences. For simplicity we assume here that $V_{\mathrm{avg}}(x, y, z) \approx \overline{V}(z)$. This energy conservation condition requires that tunneling into higher-lying states occurs further away from the surface. Due to the rapid, over-exponential decay of wave functions, the overall contribution of higher-lying states is effectively dampened. This relieves us from making *ad hoc* assumptions on which states are relevant for tunneling. This is only working thanks to the accurate description of the decaying tails obtained from EXTRA.

Combining Eqs. (14) and (15), the FIM contrast is proportional to

$$F(x, y) = \sum_{i\sigma\mathbf{k}} w_{\mathbf{k}} |\psi_{i\mathbf{k}}(x, y, z_{i\sigma\mathbf{k},I})|^2 \qquad (16)$$

where the sum runs over states above the Fermi level. The evaluation height $z_{i\sigma\mathbf{k},I}$ is implicitly defined by

$$\overline{V}(z_{i\sigma\mathbf{k},I}) = \epsilon_{i\sigma\mathbf{k}} + I \;. \qquad (17)$$

In practice, we run a search on the discrete z grid, and then linearly interpolate the DOS between the discrete z points.

In the following, we will treat the ionization energy I as a tunable parameter to evaluate the FIM contrast at different heights, namely for I=10 eV, 15 eV, and 21.5 eV (the ionization energy of Ne). Note that increasing I by 5 eV shifts the evaluation region by 2.4 bohr in a field of 40 V/nm. Fig. 8 illustrates the results. In the upper row, we show results from the original DFT wave functions. At ionization energies of 10 eV and 15 eV, there is a single bright spot arising from Ta, while at a more realistic ionization energy of 21.5 eV, the simulated contrast contains only noise. In the bottom row, obtained with EXTRA results, also the 21.5 eV contrast is very clear. At low ionization energies, there are also weak signals from the other surface atoms (Ni), but these are absent at higher energies. We note that this finding is not observed in the experiment, which clearly images Ni atoms even near Ta atoms. The reason for this strong exaggeration of brightness contrast is not entirely clear. We suspect that an adsorbed imaging gas layer present in the experiment may enhance spatial resolution. We will investigate this in more detail in a forthcoming publication.

Fig. 9 presents line scans of the simulated FIM images across the Tantalum atom. It clearly indicates the stable performance of our algorithm EXTRA over several orders of magnitude. At higher ionization energy of 21.5 eV the partial DOS from DFT differs by 2 orders of magnitude with respect to the expected true signal from EXTRA. The simulated FIM contrast is hence strongly influenced by the extrapolation of wave-function tails. The comparison of different ionization energies shows that all features become broader with increasing ionization energy (and hence increasing distance from the surface). Also, the relative contrast clearly changes. This highlights that one has to simulate using the correct ionization energy to do a quantitive comparison with the experiment.

IV. CONCLUSION

In this work, we have laid out the foundations for an accurate computation of tunneling-related contrast in field ion microscopy based on state-of-the-art density functional theory. For this, we apply the Tersoff-Hamann approximation known from scanning tunneling microscopy to the characteristic situation of tunneling into imaging gas atoms hovering above the surface in the presence of a very strong field. We identified the numerical accuracy of wave functions from the global solvers employed in plane wave DFT codes as a major limitation, and developed a novel algorithm, termed EXTRA, to recompute these tails in a very robust manner over many orders of magnitude. Equipped with this algorithm, we demonstrate for a prototypical case, Ta in Ni, that we can simulate FIM contrast maps at realistic ionization energies with practically no noise. This new scheme paves the way to

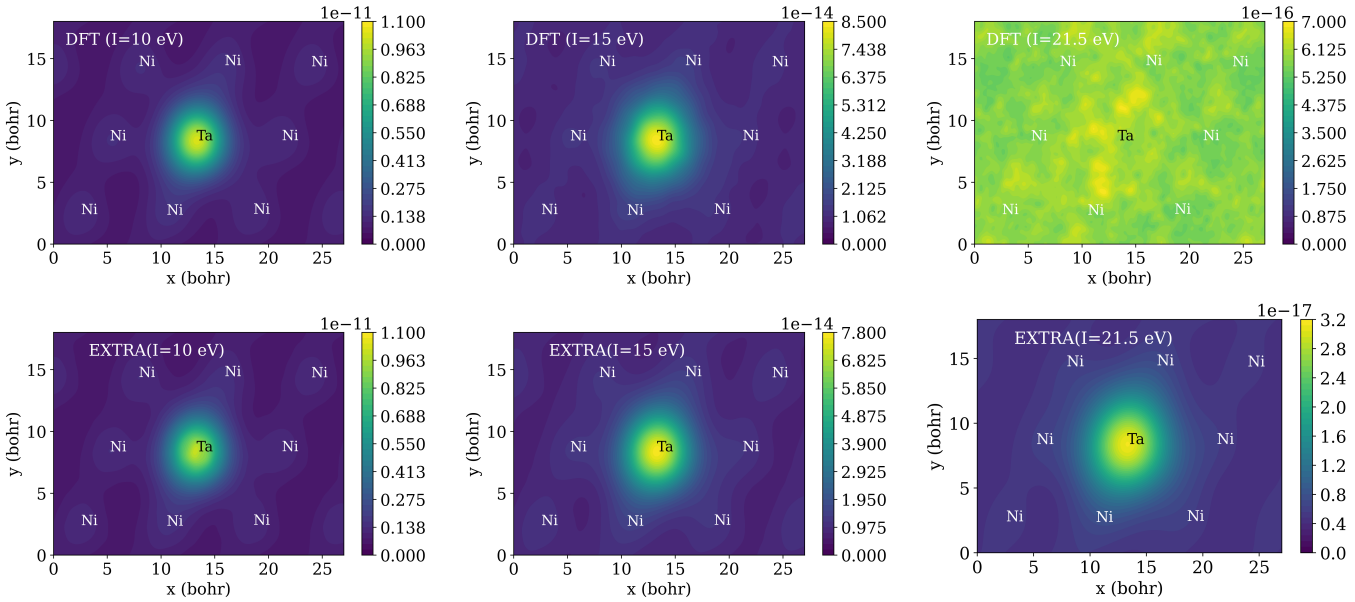

FIG. 8: Simulated FIM images of Ta-Ni(012) for different ionization energies of 10 eV, 15 eV and 21.5 eV. Top row: partial DOS obtained from the original DFT wave functions. Bottom row: refined results from EXTRA. In-plane positions of the top layer atoms are indicated in the graph.

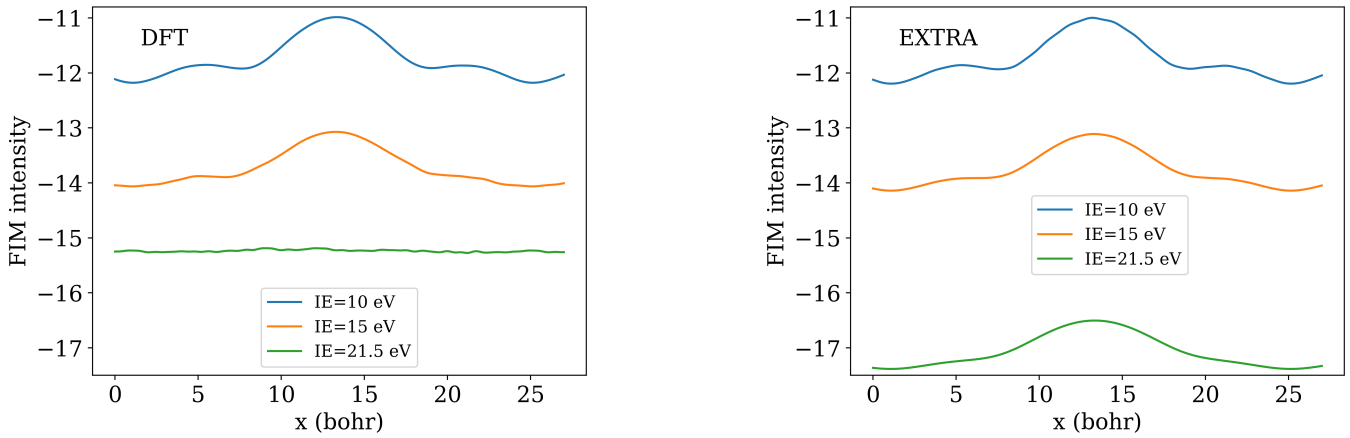

FIG. 9: 1D line scans of simulated FIM intensity from Fig. 8 on a log scale. The line runs along x across the Ta position.

systematically address open questions of contrast generation in FIM. We note that the applicability of the EXTRA the algorithm is not limited to these cases but maybe employed in other surface situations where the tails of the wave functions are of interest, e.g., in overcoming tail shape limitations when localized orbitals are used as a basis set.

ACKNOWLEDGEMENT

The authors like to thank Felipe M. Morgado and Baptiste Gault for valuable discussions. We further thank the pyiron developers, notably Marvin Poul, for their continuous technical support. SB gratefully acknowledges financial support from the International Max Planck Research School for Sustainable Metallurgy (IMPRS SusMet).

Appendix A: Electrostatic potential computed via Poisson equation

The second derivative of the electrostatic potential relates to the local charge density in Poisson's equation

$$\nabla^2\phi(\mathbf{r}) = -\frac{\rho(\mathbf{r})}{\epsilon_0} \tag{A1}$$

If in-plane Fourier transform is applied along with periodic boundary conditions denoted by (k_x, k_y) where $k = \sqrt{k_x^2 + k_y^2}$ and perpendicular to z, Eq. (A1) becomes separable as

$$\frac{\partial^2}{\partial z^2} V(k_x, k_y, z) = |\mathbf{k}|^2 V(k_x, k_y, z) - \frac{\rho(k_x, ky, z)}{\epsilon_0} \quad \text{(A2)}$$

The solution in the charge-free region is

(i) if $|\mathbf{k}| = 0$

$$V(kx = 0, ky = 0, z) = D + E_z z \quad \text{(A3)}$$

indent for constant electric field E_z, and

(ii) if $|\mathbf{k}| > 0$

$$V(k_x, k_y, z) = D + C_1 e^{-|\mathbf{k}|z} + C_2 e^{|\mathbf{k}|z} \; . \quad \text{(A4)}$$

Of course, any non-zero potential variation must be matched by charges on the counter electrode. For an ideal metallic plate-like counter electrode far away, only a homogeneous surface charge is possible that accommodates the average field E_z. Therefore, only the decaying solution $e^{-|\mathbf{k}|z}$ must be considered for $|\mathbf{k}| > 0$.

Appendix B: Derivation of the Generalized Numerov algorithm

The Kohn-Sham equation in three dimensions can be expressed as

$$\frac{1}{2}\frac{\partial^2}{\partial z^2}\psi(\mathbf{x}, z) + \left\{\epsilon - \hat{V}(z)\right\}\psi(\mathbf{x}, z) = 0 \quad \text{(B1)}$$

with the in-plane operator

$$\hat{V}(z) = -\frac{1}{2}\left(\frac{\partial^2}{\partial x^2} + \frac{\partial^2}{\partial y^2}\right) + V(\mathbf{x}, z) \; . \quad \text{(B2)}$$

$\mathbf{x}$ comprises the in-plane coordinates in either real or mixed space. The in-plane operator is strictly local along the z direction, but within the plane, it is semilocal (in real space) or even non-local (in mixed space). Next, we discretize along the z direction with a spacing h, i.e., $z_n = nh$, and Taylor series expansion of ψ to fifth order (with $\psi_n = \psi(\mathbf{x}, z_n)$):

$$\begin{aligned}\psi_{n\pm1} = \psi_n &\pm h\frac{\partial}{\partial z}\psi_n + \frac{h^2}{2}\frac{\partial^2}{\partial z^2}\psi_n \\ &\pm \frac{h^3}{6}\frac{\partial^3}{\partial z^3}\psi_n + \frac{h^4}{24}\frac{\partial^4}{\partial z^4}\psi_n \\ &\pm \frac{h^5}{120}\frac{\partial^5}{\partial z^5}\psi_n + \mathcal{O}(h^6)\end{aligned} \quad \text{(B3)}$$

Adding the equations for ψ_{n+1} and ψ_{n-1} makes the odd derivatives vanish. To evaluate the term involving the 4th derivative we act on Eq. B1 with $1 + \frac{h^2}{12}\frac{\partial^2}{\partial z^2}$ which gives

$$\frac{\partial^2}{\partial z^2}\psi_n + \frac{h^2}{12}\frac{\partial^4}{\partial z^4}\psi_n + \left\{\epsilon - \hat{V}(z)\right\}\psi_n + \frac{h^2}{12}\frac{\partial^2}{\partial z^2}\left\{\epsilon - \hat{V}(z)\right\}\psi_n = 0 \quad \text{(B4)}$$

Substituting for $\frac{\partial^2}{\partial z^2}\psi_n + \frac{h^2}{12}\frac{\partial^4}{\partial z^4}\psi_n$ and evaluate $\frac{\partial^2}{\partial z^2}\left\{\epsilon - \hat{V}(z)\right\}\psi_n$ gives

$$\frac{\partial^2}{\partial z^2}\left\{\epsilon - \hat{V}(z_n)\right\}\psi_n = \frac{\left\{\epsilon - \hat{V}(z_{n+1})\right\}\psi_{n+1} + \left\{\epsilon - \hat{V}(z_{n-1})\right\}\psi_{n-1} - 2\left\{\epsilon - \hat{V}(z_n)\right\}\psi_n}{h^2} \quad \text{(B5)}$$

With this substitution, one can rearrange terms to arrive at

$$\left[1 + \frac{1}{6}h^2\left\{\epsilon - \hat{V}(z_{n+1})\right\}\right]\psi_{n+1} = 2\left[1 - \frac{5}{6}h^2\left\{\epsilon - \hat{V}(z_n)\right\}\right]\psi_n - \left[1 + \frac{1}{6}h^2\left\{\epsilon - \hat{V}(z_{n-1})\right\}\right]\psi_{n-1} \quad \text{(B6)}$$

[1] E. W. Müller, Das Feldionenmikroskop, Zeitschrift für Physik **131**, 136 (1951).

[2] E. W. Müller, Resolution of the atomic structure of a metal surface by the field ion microscope, Journal of Applied Physics **27**, 474 (1956).

[3] D. Brandon, The resolution of atomic structure: recent advances in the theory and development of the field ion microscope, British Journal of Applied Physics **14**, 474 (1963).

[4] J. Chen, *Introduction to Scanning Tunneling Microscopy*

Third Edition, Vol. 69 (Oxford University Press, USA, 2021).
[5] A.-S. Lucier, H. Mortensen, Y. Sun, and P. Grütter, Determination of the atomic structure of scanning probe microscopy tungsten tips by field ion microscopy, Physical Review B **72**, 235420 (2005).
[6] S. Katnagallu, F. F. Morgado, I. Mouton, B. Gault, and L. T. Stephenson, Three-dimensional atomically resolved analytical imaging with a field ion microscope, Microscopy and Microanalysis **28**, 1264 (2022).
[7] F. Vurpillot, M. Gilbert, and B. Deconihout, Towards the three-dimensional field ion microscope, Surface and Interface Analysis: An International Journal devoted to the development and application of techniques for the analysis of surfaces, interfaces and thin films **39**, 273 (2007).
[8] M. Dagan, B. Gault, G. D. Smith, P. A. Bagot, and M. P. Moody, Automated atom-by-atom three-dimensional (3d) reconstruction of field ion microscopy data, Microscopy and Microanalysis **23**, 255 (2017).
[9] C. Speicher, W. Pimbley, M. Attardo, J. Galligan, and S. Brenner, Observation of vacancies in the field-ion microscope, Physics letters **23**, 194 (1966).
[10] J. Park, H. Huang, R. Siegel, and R. Balluffi, A quantitative study of vacancy defects in quenched tungsten by combined field-ion microscopy and electrical resistometry, Philosophical Magazine A **48**, 397 (1983).
[11] S. Katnagallu, L. T. Stephenson, I. Mouton, C. Freysoldt, A. P. Subramanyam, J. Jenke, A. N. Ladines, S. Neumeier, T. Hammerschmidt, R. Drautz, *et al.*, Imaging individual solute atoms at crystalline imperfections in metals, New Journal of Physics **21**, 123020 (2019).
[12] B. Klaes, R. Lardé, F. Delaroche, C. Hatzoglou, S. Parvianien, J. Houard, G. Da Costa, A. Normand, M. Brault, B. Radiguet, *et al.*, Development of wide field of view three-dimensional field ion microscopy and high-fidelity reconstruction algorithms to the study of defects in nuclear materials, Microscopy and Microanalysis **27**, 365 (2021).
[13] S. Katnagallu, M. Dagan, S. Parviainen, A. Nematollahi, B. Grabowski, P. A. J. Bagot, N. Rolland, J. Neugebauer, D. Raabe, F. Vurpillot, M. P. Moody, and B. Gault, Impact of local electrostatic field rearrangement on field ionization, J. Phys. D: Appl. Phys. **51**, 105601 (2018).
[14] R. G. Forbes, Field-ion image formation, Nature Physical Science **230**, 165 (1971).
[15] R. G. Forbes, A theory of field-ion imaging: I. A quasi-classical site-current formula, Journal of Microscopy **96**, 57 (1972).
[16] R. G. Forbes, A theory of field-ion imaging: II. On the origin of site-current variations*, Journal of Microscopy **96**, 63 (1972).
[17] S. S. Katnagallu, *On chemically sensitive atomic scale imaging*, doctoralthesis, Ruhr-Universität Bochum, Universitätsbibliothek (2018).
[18] J. Tersoff and D. R. Hamann, Theory of the scanning tunneling microscope, Physical Review B **31**, 805 (1985).
[19] C. Freysoldt, A. Mishra, M. Ashton, and J. Neugebauer, Generalized dipole correction for charged surfaces in the repeated-slab approach, Phys. Rev. B **102**, 045403 (2020).
[20] M. C. Payne, M. P. Teter, D. C. Allan, T. Arias, and a. J. Joannopoulos, Iterative minimization techniques for ab initio total-energy calculations: molecular dynamics and conjugate gradients, Reviews of modern physics **64**, 1045 (1992).
[21] F. F. Morgado, S. Katnagallu, C. Freysoldt, B. Klaes, F. Vurpillot, J. Neugebauer, D. Raabe, S. Neumeier, B. Gault, and L. T. Stephenson, Revealing atomic-scale vacancy-solute interaction in nickel, Scripta Materialia **203**, 114036 (2021).
[22] D. Sholl and J. A. Steckel, *Density functional theory: a practical introduction* (John Wiley & Sons, 2011).
[23] M. Purevkhuu and V. Korobov, On one implementation of the numerov method for the one-dimensional stationary schrödinger equation, Physics of Particles and Nuclei Letters **18**, 153 (2021).
[24] D. Bennett, Numerical solution of time-independent 1-d schrodinger equation (2015).
[25] D. Kenhere, Bound state of one dimensional potential by numerov method, Phys. Educ , 55 (2007).
[26] T. Simos, A new numerov-type method for the numerical solution of the schrödinger equation, Journal of mathematical chemistry **46**, 981 (2009).
[27] M. Pillai, J. Goglio, and T. G. Walker, Matrix numerov method for solving schrödinger's equation, American Journal of Physics **80**, 1017 (2012).
[28] P. Virtanen, R. Gommers, T. E. Oliphant, M. Haberland, T. Reddy, D. Cournapeau, E. Burovski, P. Peterson, W. Weckesser, J. Bright, *et al.*, Scipy 1.0: fundamental algorithms for scientific computing in python, Nature methods **17**, 261 (2020).
[29] C. T. Kelley, *Iterative methods for linear and nonlinear equations* (SIAM, 1995).
[30] S. Boeck, C. Freysoldt, A. Dick, L. Ismer, and J. Neugebauer, The object-oriented dft program library s/phi/nx, Computer Physics Communications **182**, 543 (2011).
[31] J. P. Perdew, K. Burke, and M. Ernzerhof, Generalized gradient approximation made simple, Phys. Rev. Lett. **77**, 3865 (1996).
[32] S. Grimme, Semiempirical GGA-type density functional constructed with a long-range dispersion correction, J. Comp. Chem. **27**, 1787 (2006).
[33] C. Freysoldt, On-the-fly parameterization of internal coordinate force constants for quasi-newton geometry optimization in atomistic calculations, Comput. Mater. Sci. **133**, 71 (2017).